

Materials Sciences Division, Lawrence Berkeley National Laboratory, and
Department of Materials Science and Engineering
University of California at Berkeley

THE IDEAL STRENGTH OF IRON

D.M. Clatterbuck¹, D.C. Chrzan^{1,2} and J.W. Morris, Jr.^{1,2}

¹ Materials Sciences Division, Lawrence Berkeley National Laboratory, and
Department of Materials Science and Engineering,
University of California, Berkeley, CA 94720

² Corresponding Author: Tel: (510) 486-5994; Fax: (510) 486-4023
E-mail address: dcchrzan@socrates.berkeley.edu (*D.C. Chrzan*)

² Corresponding Author: Tel: (510) 486-6482; Fax: (510) 486-4023
E-mail address: jwmorris@uclink4.berkeley.edu (*J.W. Morris, Jr.*)

March 2003

Accepted for Publication:
Elsevier Science

This work was supported by the Director, Office of Science, Office of Basic Energy Sciences, of the Department of Energy under contract No. DE-AC03-76SF00098.

The Ideal Strength of Iron

D. M. Clatterbuck, D. C. Chrzan and J. W. Morris Jr.

Department of Materials Science and Engineering, UC Berkeley and
Materials Sciences Division, Lawrence Berkeley National Lab, Berkeley CA 94609

ABSTRACT

The ideal strength of a material can be defined as the stress that causes an infinite defect-free perfect crystal to become mechanically unstable. The ideal strength is of interest because it sets a firm upper bound on the mechanical strength the material can attain. It is also approached experimentally in situations where there are few mobile defects. The present paper is concerned with the ideal strength of iron. We specifically compute the ideal tensile strength of iron for tension along $\langle 001 \rangle$, the weak direction, and the ideal shear strength for relaxed shear in the $\langle 111 \rangle \{112\}$ and $\langle 111 \rangle \{110\}$ systems. We also consider the influence of pressure on the strength. The computation is done *ab initio* using the Projector Augmented Wave Method within the framework of density functional theory and the generalized gradient approximation in order to account for the magnetism of the material. The fact that iron can have a high tensile strength is puzzling. Because Fe has a stable fcc phase (at least at moderate temperature) simple models suggest that it should be very weak in tension on $\langle 100 \rangle$. That it is not turns out to be due to the difference in magnetic character between the bcc and fcc phases, which has the consequence that iron behaves like a “typical” bcc metal in both its tensile and shear behavior.

INTRODUCTION

For almost three millennia the element Fe and its alloys have provided the most commonly used structural metals, and remain the materials of choice for a large fraction of all engineering structures and devices. There are three basic reasons why this is true. First, Fe is common in the earth’s crust, and is relatively easy to extract from its ores. Second, Fe has reasonable inherent strength, and can be alloyed or processed so that it becomes even stronger. Third, Fe (or steel) is a very flexible material that can be made soft for forming, or hard for structural strength by fairly straightforward changes in the way it is processed. The strength of Fe is a prerequisite. If it did not lend itself to the creation of alloys that are “as strong as steel”, it would not be widely used.

Advances in computational techniques and computing machines have recently made it possible to compute the ideal strength of a crystalline material – the stress that drives the crystal lattice itself unstable and sets an upper bound on the strength the material can possibly have [1,2]. When these techniques are applied to Fe, as was done for the first time in the work reported here [3,4], a couple of surprises emerge. First, Fe is not really all that strong. Second, it is surprising that Fe is as strong as it is.

These statements can be based on a simple model that is derived from the dominant role of symmetry in determining the ideal strength, as is well established from first-principles calculations [2,5]. The energy of a deformed crystal depends on the six independent components of the strain and is, hence, a 6-dimensional hypersurface in a 7-dimensional space. The local extrema and saddle points on this hypersurface almost always correspond to structures with high symmetry. The configurations of greatest interest are the saddle points on the energy surface that neighbor the initial state. For a given load geometry (stress state) the crystal deforms along a particular path on the strain-energy surface as the load is increased. The stress required to drive the system is related to the local slope of the energy surface in the direction of travel. The ideal strength is determined by the steepest slope along the path between the initial state and the first saddle point.

The steepest slope corresponds to the maximum stress; the crystal is elastically unstable as soon as the point of maximum stress is passed.

To understand the ideal strength it is necessary to identify the relevant saddle point structures. Four such structures have been identified in studies of the ideal strengths of bcc metals: the fcc structure, the simple cubic (sc) structure, a body centered tetragonal (bct) structure, and a base centered orthorhombic structure [6-8]. For example, relaxed shear of a bcc metal in the "easy" $\langle 111 \rangle$ direction on the $\{112\}$ or $\{110\}$ plane generates a stress-free bct structure [8]. Because the $\langle 111 \rangle \{112\}$ shear system is not symmetric in the sign of the shear direction, it is also possible to move from a bcc structure to a base centered orthorhombic structure by shearing in the "hard" direction. Uniaxial tension in the $\langle 111 \rangle$ direction takes a bcc structure to a sc structure [6,8], while $\langle 001 \rangle$ tension moves it from bcc either to fcc (the Bain transformation in Fig. 1 [2]) or to bct (the same stress-free bct structure encountered in shear [7]). The competition between the two possible paths that can be reached by $\langle 001 \rangle$ tension has the result that, while most bcc crystals (Mo, W) are governed by the instability associated with the fcc structure and, ideally, fail in cleavage, at least one (Nb) becomes unstable with respect to evolution toward the bct saddle point and fails in shear [7].

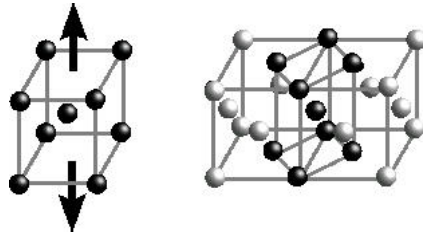


Figure 1: The bcc crystal structure becomes the fcc structure after elongation along the $\langle 100 \rangle$ direction.

Ab initio total energy calculations of the ideal tensile strengths of unconstrained bcc metals show that they are weakest when pulled in a $\langle 001 \rangle$ direction [2] (unsurprisingly, $\{001\}$ is the dominant cleavage plane in bcc metals). A constant volume tensile strain along $\langle 001 \rangle$ converts the bcc structure into fcc at an engineering strain of about 0.26 (the 'Bain strain', Fig. 1). Since both structures are unstressed by symmetry, the tensile stress must pass through at least one maximum along the transformation path. If we follow Orowan [9] in assuming a single extremum (the solid line in Fig. 2), and fit the stress-strain curve with a sinusoid that has the correct modulus at low strain, the ideal tensile strength is approximately

$$\sigma_m = 0.08 E_{\langle 100 \rangle} \quad (1)$$

in good agreement with *ab initio* calculations (for example, $\sigma_m = 30 \text{ GPa} = 0.072 E_{\langle 100 \rangle}$ for W [10]). Since the modulus of Fe is significantly less than that of other transition metals, such as W, Mo and Ta, the upper bound on its strength is smaller as well.

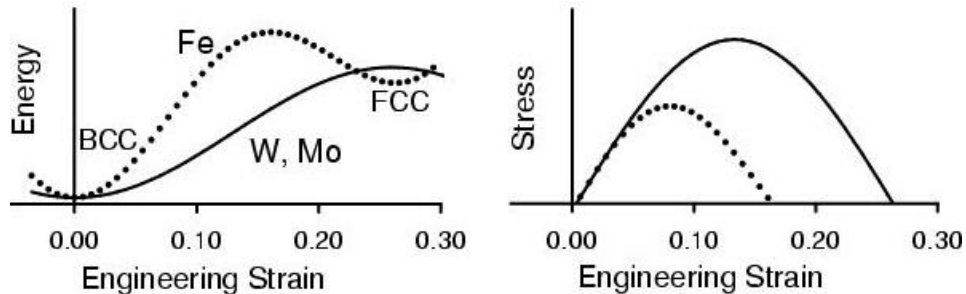


Figure 2: The energy as a function of strain has an extremum at the fcc structure which can be a local maximum (solid line) or minimum (dotted line). Assuming sinusoidal form, the inflection point governing the ideal strength falls at a much lower strain in the latter case, and the ideal strength is significantly less.

But a second problem intrudes when we extend this analysis to iron [3]. The fcc phase in Fe is known to have an energy only slightly above that of bcc and is at least metastable at low temperature. In fact, the thermomechanical treatments that are used to process structural steel (particularly including the many developed or explored by Gareth Thomas) rely on the ease of transforming it from bcc to fcc and back again. If we assume a metastable fcc phase connected by a continuous strain-energy curve (the dotted line in Fig.

2), the tensile instability intrudes at a much smaller strain, and the ideal strength should be only about 6 GPa (versus 12 GPa based on an unstable fcc). This number is too small to be credible. Since tensile stresses that are several times the yield strength are developed ahead of crack tips in elastic-plastic materials, steels with yield strengths much above 1 GPa would necessarily be brittle. In fact, steels with much larger yield strengths have high fracture toughness and considerable ductility.

A possible resolution of this paradox is suggested by the work of Herper et al. [11]. They computed the energies of Fe for various magnetic states and lattice strains. Their calculations suggest that the energy of ferromagnetic Fe increases monotonically if it is distorted toward an unstable, ferromagnetic fcc, which can be stabilized by transforming into a complex antiferromagnetic state. This has the consequence that the low energy antiferromagnetic fcc phase is a minimum rather than a saddle point on the strain-energy surface of Fe. While Herper, et al. [11] did not investigate the point (they had other interests), this suggests the possibility that ferromagnetic Fe may become mechanically unstable under $\langle 100 \rangle$ tension before encountering the magnetic transition that converts it into the antiferromagnetic state that stabilizes fcc. If this is the case, Fe can have the mechanical behavior of a typical bcc metal, while still having a metastable fcc structure that is stabilized by a late magnetic transition. That is, it can be both strong and easy to process.

As we shall show below, this is the apparent explanation for the fact that Fe has both a useful tensile strength and an fcc phase that facilitates processing. Going further, we shall establish that Fe naturally fails in cleavage on $\{100\}$ planes and compute its tensile and shear strengths. Finally, we consider how the strength of Fe is affected by superimposed hydrostatic stress as encountered, for example, at the tip of a sharp crack.

COMPUTATIONAL METHODS

To compute the ideal strength of Fe we must include magnetic interactions. These are non-local, and considerably complicate the problem. In particular, the non-local magnetic interactions have the consequence that the local density approximation cannot be used. In fact, computations based on the local density approximation predict that the ground state of Fe should be a non-magnetic close packed structure rather than a bcc ferromagnet. The use of the generalized gradient approximation (GGA) has been shown to correct this problem [12]. Full Potential Linearized Augmented Plane Wave (FLAPW) calculations which make no further approximations beyond the GGA (assuming convergence of the basis set, charge density representation and Brillouin Zone integration) are probably the most reliable [13]. Unfortunately, in order to efficiently relax the stresses orthogonal to the applied stress, the stresses on the unit cell must be directly computable, and there are no implementations of the FLAPW method known to us that can do this in a straightforward way. For this reason we selected the Projector Augmented Wave (PAW) method, originally developed by Blochl [14], for this work. PAW is an approximation to FLAPW that captures most of its important features and can be formulated to calculate local stresses by the Hellman-Feynman method. We also performed some calculations using the FLAPW method as a check on the accuracy of the results. The two methods are in reasonable agreement. The details of the computation are given in ref. [4].

The ideal strength was computed for uniaxial stress in tension or shear. The lattice vectors were incrementally deformed in the direction of the imposed stress, and at each step the structure was relaxed until the stresses orthogonal to the applied stress vanished, as indicated by those components of the Hellman-Feynman stresses being less than 0.15 GPa [15]. Because there is no unique measure of strain for a given finite deformation, we describe our deformations in terms of the engineering strain from the equilibrium structure. The initial set of lattice vectors \mathbf{r}^α ($\alpha=1,2,3$) in an orthogonal coordinate system become the vectors $\mathbf{r}^{\alpha'}$ after homogeneous deformation by the transformation $r_i^{\alpha'} = r_i^\alpha + D_{ij} r_j^\alpha$. From this transformation, we define the strain to be $e_{ij} = [D_{ij} + D_{ji}]/2$. As is customary, we redefine the shear strains to be $\gamma_{ij} = 2e_{ij}$ for $i \neq j$. While the engineering strain is convenient for describing the change in the lattice vectors from their original configuration, the Cauchy (true) stress cannot be calculated from the derivative of the free energy with respect to this strain measure. To compute the Cauchy stress we take the derivative of the free energy with respect to the incremental strain from a nearby reference state, yielding a stress that converges to the thermodynamic definition of the Cauchy stress in the limit of small incremental strain.

It should be noted that the ideal strengths determined from these calculations are for quasi-static deformation at 0K, and that other dynamic instabilities such as soft phonons may lower the ideal strength.

EQUILIBRIUM STRUCTURES

We chose to compute the ideal strength with the Projector Augmented Wave (PAW) method because of its computational efficiency and its ability to treat lattice stress. To check the accuracy of the method, we computed the energy as a function of volume for several magnetic structures and compared the results to calculations done using the FLAPW method as well as with available experimental data. The magnetic structures included the following: bcc ferromagnet (FM), fcc ferromagnet (FM), fcc antiferromagnet (AFM), fcc non-magnetic (NM). The results are plotted in Fig. 3. The results for the ferromagnetic bcc phase are tabulated in Table 1.

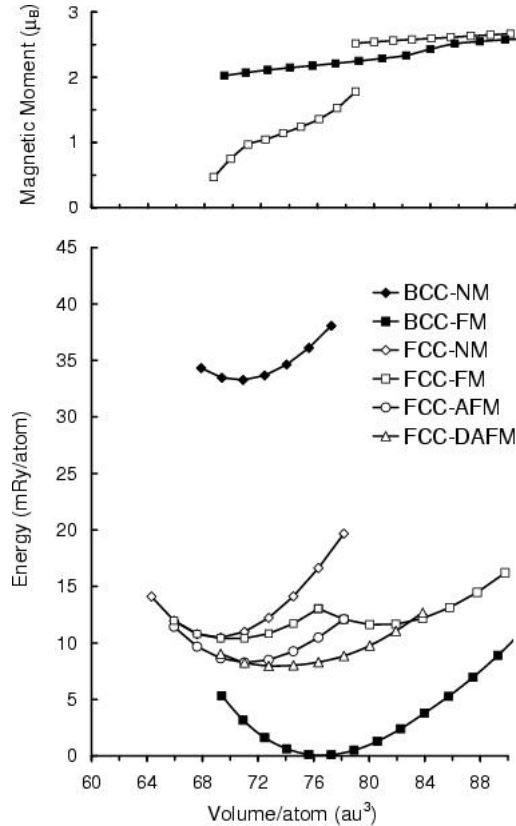


Figure 3: The energy and magnetic moment per atom as functions of volume computed using the PAW method for Fe in the bcc (filled symbols) and fcc (open symbols) crystal structures for several magnetic states: (diamonds) non-magnetic (NM), (squares) ferromagnetic (FM), (circles) antiferromagnetic (AFM), and (triangles) double period antiferromagnetic (DAFM). The discontinuity in the fcc FM curve separates two distinct phases with different magnetic moments.

In general the agreement between the two computational methods is good. Comparing the PAW and FLAPW methods, the equilibrium volumes of the various phases agree to within 1%. The elastic constants of the bcc FM phase agree to within 3% with the exception of c_{44} , which has a discrepancy of 13%. Compared with experimental measurements of the bcc phase at 4 K, the PAW calculations predict a lattice parameter that is too small by 1% and elastic constants which are generally about 10% too large suggesting a slight over-binding (the only discrepancy being c_{44} which is 18% too small). From the computed elastic constants, the relaxed tensile modulus in the $\langle 001 \rangle$ direction, $E_{\langle 001 \rangle} = 1/s_{11}$, is found to be about 29% too large, while the relaxed shear modulus in the $\langle 111 \rangle$ direction, $G_{\langle 111 \rangle} = 3c_{44}(c_{11}-c_{12})/(4c_{44}+c_{11}-c_{12})$, is about 18% too large.

In regards to the magnetic properties, both the PAW and FLAPW methods correctly predict that the ground state is the bcc ferromagnetic phase with a magnetic moment of 2.20 μ_B and 2.15 μ_B respectively as compared to the experimental value of 2.22 μ_B [1]. Both sets of calculations also predict that the ferromagnetic

fcc phase undergoes a pressure-induced, first order phase transformation at a volume of 76-77 au³/atom from a low-volume, low-moment phase to a high-volume, high-moment phase. The groundstate magnetic structure of fcc Fe has been debated on theoretical grounds extensively in the literature. While bulk fcc Fe is difficult to achieve experimentally at low temperature, there is some probative experimental data on the magnetic state of nearly pure Fe in the fcc crystal structure. It is possible to stabilize fcc Fe by growth as a thin epitaxial film or as small precipitates in a copper matrix. Tsunoda [17,18] found that small fcc precipitates in Cu that are almost pure Fe have a spiral spin density wave (SSDW) ground state. Knopfle et al. [19] have recently published calculations using the modified augmented spherical wave method that show good agreement with this experimental data. Their minimum energy fcc structure has a spiral vector of $\mathbf{q}=(0.15,0,1)$ with an energy which lies <1 mRy below the AFM phase and has a slightly larger equilibrium volume than the AFM phase.

Due to the complexity involved in treating non-collinear magnetism, in the present work we have used collinear structures as approximate representations of the true magnetic ground state. Herper, Hoffmann, and Entel [11] proposed using a collinear double period antiferromagnetic structure (DAFM) as an approximate to the non-collinear ground state in fcc Fe. In this structure the spins on (002) planes are oriented up-up-down-down. The energy as a function of volume of this structure is plotted in Figure 4 and we see that it is located <1 mRy below the AFM phase and has a similar equilibrium volume. The spiral spin density wave studied by Knopfle, et al. [19] has an energy only slightly below this.

TABLE 1

Lattice parameters, volumes, relative energies and elastic constants from PAW and FLAPW calculations as well as experiment. All energies are relative to the FM bcc phase which is taken as 0. Experimental elastic constants at 4K are from [20] and the experimental lattice parameter extrapolated to 4 K is from Ref. [21].

	PAW	FLAPW	PAW-FLAPW %Error	Experiment (4K)	PAW-Experiment %Error
bcc-FM					
$V_o(\text{au}^3)$	76.47	76.20	0.4%	78.94	-3.1%
$a_o(\text{\AA})$	2.830	2.827	0.1%	2.86	-1.1%
B (GPa)	194	196	-1.0%	174	11.5%
c_{11} (GPa)	286	289	-0.9%	245	16.9%
c_{12} (GPa)	147	152	-3.43%	139	5.9%
c_{44} (GPa)	99	114	-12.8%	122	-18.5%
$E_{<100>}$ (GPa)	187	184	1.5	144	29.2%
$G_{<111>}$ (GPa)	77	78.9	-1.9%	65	18.4%

IDEAL STRENGTH IN TENSION

We first consider the ideal strength in tension. Since previous calculations and symmetry arguments suggest $\langle 001 \rangle$ is the weakest direction in tension for bcc metals [2], we have focused on the ideal strength in this direction.

Tetragonal versus orthorhombic instability

There are two possible deformation paths for uniaxial tension in the $\langle 001 \rangle$ direction (Fig. 4). An infinitesimal strain in the $\langle 001 \rangle$ direction distorts the crystal into a body centered tetragonal (bct) configuration. If we compute the deformation path under the constraint that the cell maintain tetragonal symmetry we obtain the results shown in Fig. 5. The energy reaches a local maximum at 28% strain in the fcc structure (c/a ratio = $\sqrt{2}$), and then it reaches a local minimum at 42% strain in a stress-free bct structure

with a c/a ratio of 1.66. The plot of tensile stress versus strain along this path has a maximum of 12.6 GPa at 15% strain. The maximum locates the elastic instability along the bcc-fcc (Bain) deformation path and corresponds, physically, to cleavage on the $\{001\}$ plane.

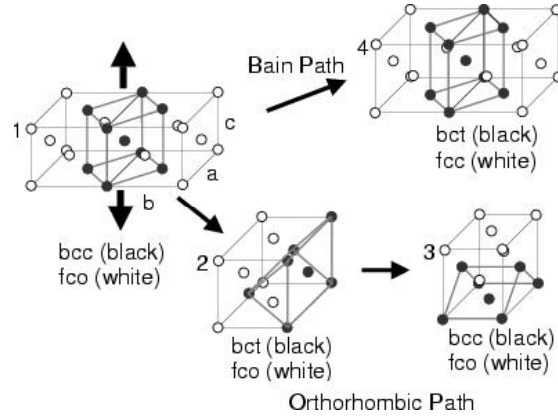


Figure 4: The geometry of the Bain path and the orthorhombic instability. If tetragonal symmetry is maintained the Bain path is followed from the bcc structure to the fcc, which is equivalent to a bct structure with a c/a ratio of $\sqrt{2}$. If the tetragonal symmetry is broken the orthorhombic path is followed and a maximum energy is reached at a special bct structure that has a c/a ratio of 1.66. The orthorhombic path eventually produces a bcc cell that is rotated relative to the original bcc cell.

The initial bct structure can also be treated as a special case of a face centered orthorhombic (fco) structure that is rotated by 45° (Fig. 4) and has a $a:b:c$ ratio of $\sqrt{2}:\sqrt{2}:1$, where we take the c -axis to lie in the direction of the applied strain. If we preserve orthorhombic symmetry (which allows the tetragonal symmetry to be broken) the deformation is coincident with the Bain path up to a strain of $\sim 18\%$, but then diverges from it. The evolution of the ratios of the orthorhombic lattice parameters along the loading path is shown at the bottom of Fig. 5 and the geometric relationship between the special crystal structures is shown in Fig. 4. At a strain of 18% the crystal spontaneously develops an orthorhombic distortion. The energy reaches a maximum at 21% strain, then falls off into a local minimum at a strain of 42%. The energy maximum along the orthorhombic path occurs at the "special" bct structure with a c/a ratio of 1.66, and the energy minimum is a bcc structure that is rotated relative to the initial bcc cell (see Fig. 4). If one refers the structure back to the bct structure with the deformation in the $[001]$ direction, the orthorhombic instability corresponds to the elastic constant c_{66} vanishing, which causes the crystal to become unstable with respect to a shear. Although the crystal is pulled in tension this instability initiates a shear failure on the $\langle 111 \rangle \{112\}$ system of the bcc crystal.

The competition between tetragonal and orthorhombic instabilities in bcc crystals was first noted by Luo, et al. [7], who found that the tetragonal instability dominates in Mo (as in W) while the orthorhombic instability intrudes in Nb. The issue is physically important, since the tetragonal instability leads to failure in tension ($\{001\}$ cleavage) while the orthorhombic instability leads to failure in shear ($\langle 111 \rangle \{112\}$ shear). Ferromagnetic Fe behaves like the conventional bcc metals, W and Mo. Its ideal strength in $\langle 001 \rangle$ tension, 12.6 GPa, is determined by the tetragonal instability and, hence, by cleavage on $\{001\}$. In keeping with this result, Fe cleaves on $\{001\}$ when tested at low temperature.

We also computed the ideal tensile strength of Fe using the FLAPW method; however, in those calculations only tetragonal structures were considered. A slightly higher ideal strength, 14.2 GPa was found, which is consistent with the larger energy difference between the bcc FM and fcc FM structures found with the FLAPW method as compared to the PAW method. The energy difference may be due to the differences in the treatment of the GGA or errors introduced by the PAW potential. The conditions of stability developed by Morris and Krenn [xx] were tested at 14% strain to check for orthogonal instabilities. No orthogonal instabilities were found at that strain, consistent with the PAW calculations. However, the elastic constant c_{66} was found to be only ~ 30 GPa, quite a bit smaller than in bcc Fe (114 GPa), which is an indication of the close proximity of the orthorhombic instability.

Assuming a sinusoidal stress-strain curve that returns to zero at the actual strain needed to reach the fcc phase, 0.286, we have

$$\sigma = \sigma_m \sin(\epsilon\pi/0.286). \quad (2)$$

Requiring that Hooke's law be satisfied for small strains: $\sigma_m = 0.286E_{\langle 001 \rangle}/\pi = 0.091E_{\langle 001 \rangle}$, where $E_{\langle 001 \rangle}$ is Young's modulus for elongation in the $\langle 001 \rangle$ direction. Eq. 2 agrees well with the results calculated here: $\sigma_m/E=0.087$ with the experimental value for $E_{\langle 001 \rangle}$, or $\sigma_m/E=0.068$ with the calculated value.

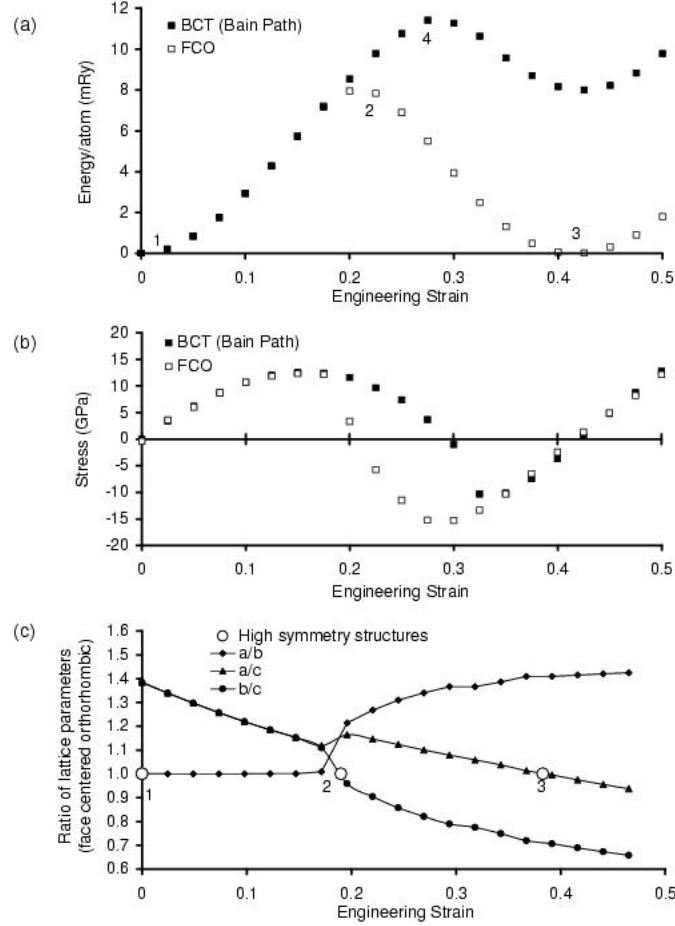


Figure 5: (a) Energy and (b) stress as a function of applied tensile strain along $\langle 001 \rangle$: (filled squares) Bain Path with tetragonal symmetry, (open square) orthorhombic path. (c) Ratios of the lattice parameters along the orthorhombic path: (filled diamond) a/b , (filled triangle) a/c , (filled circle) b/c . Numbers and open circles in (a) and (c) indicate special structures with high symmetry that are shown schematically in Figure 6.

Magnetic instabilities

The results to this point have only considered ferromagnetic (FM) states; however, the fact that Fe has a metastable, antiferromagnetic fcc phase at low temperature suggests that it must become unstable with respect to magnetic transitions at large strains. We will now consider this possibility.

As discussed above, we approximate the magnetic structures of fcc Fe by collinear structures for computational simplicity. In addition, we used a scalar relativistic approximation that does not include the effects of spin-orbit coupling. However, our earlier calculations using the FLAPW method showed that this makes a negligible effect on the energy differences between various magnetic structures. In the actual calculation we fix the magnetic structure and relax the lattice into the required stress state. We then increment the strain to obtain the energy and stress as a function of the strain, relaxing the lattice at each step along the path. This entire process is then repeated for various magnetic structures.

Fig. 6 shows the calculated energy as a function of strain for Fe in the FM, AFM, DAFM and low-spin FM structures. We have studied both bct and fco structures and found that the AFM and LSFM structures remain tetragonal while the DAFM and FM structures undergo a transformation to the fco structure at different points along the loading path. The DAFM structure is preferred to FM Fe for strains above about ~20%. This result suggests that the ideal strength is not compromised by magnetic instability since the structural instability ($\{001\}$ cleavage) occurs at about 15% strain, well before the magnetic transition intrudes. Thus, the ideal strength in $\langle 001 \rangle$ tension is ~12.6 GPa and is set by a tensile elastic instability along the Bain path from bcc to fcc. The stability of fcc iron is made possible by a magnetic phase transition at larger strains that does not affect the ideal strength.

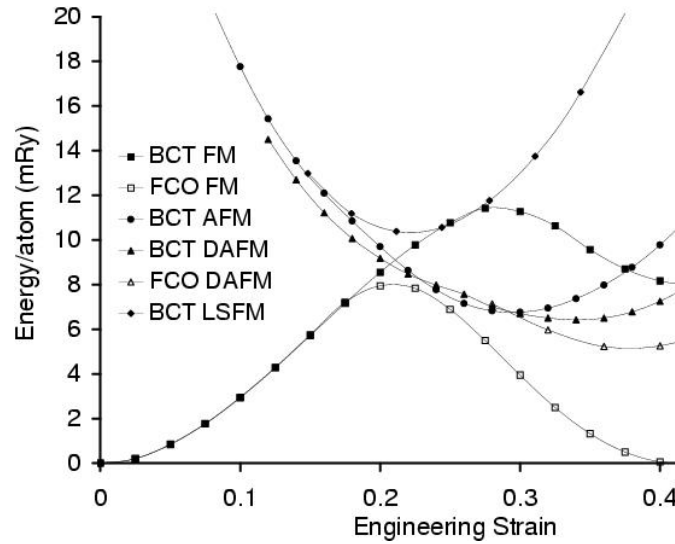


Figure 6: Energy versus strain in the $\langle 001 \rangle$ direction for various magnetic structures: (solid square) bct-FM, (open square) fco-FM, (filled triangle) bct-DAFM, (open triangle) fco-DAFM, (filled circle) bct-AFM, (filled diamond) bct-LSFM. The fco-AFM and fco-LSFM structures follow paths identical to bct-AFM and bct-LSFM respectively and are not shown. A magnetic phase transformation is seen near 20% strain.

Comparison with previous calculations and experiment

Several previous authors have studied the energy as function of tetragonality for Fe, but have not determined the ideal strength [11,22]. Friak et al. [23] independently calculated the ideal tensile strength along the tetragonal loading path using the FLAPW method and found a strength of 12.7 GPa, in good agreement with our results from the PAW method and slightly lower than our calculations using the FLAPW method (14.2 GPa). While the use of different GGA formulations in the three cases makes exact comparison difficult, the differences are within the error range for density functional methods. To our knowledge, the only attempt to measure the ideal tensile strength of Fe was by Brenner [24] who tested Fe whiskers in tension. He measured a value of ~5 GPa for tension in the $\langle 001 \rangle$ direction. While this value is considerably lower than the calculated ideal strength, the failure initiated at the surface and, therefore, does not represent bulk strength. The measured value of the strength in the $\langle 111 \rangle$ direction was 13 GPa, but it is expected that the ideal strength of bcc metals in the $\langle 111 \rangle$ direction is significantly larger than in the $\langle 001 \rangle$ direction [2].

IDEAL STRENGTH IN SHEAR

Shear strength of FM bcc Fe

We computed the ideal shear strength of Fe for two common slip systems: $\langle 111 \rangle \{112\}$ and $\langle 111 \rangle \{110\}$. The energy and the stress are plotted as functions of the shear strain for the two systems in Fig. 7. We note that the ideal strength in the easy direction is very similar for the two slip systems, 7.2 GPa for $\langle 111 \rangle \{112\}$ and 7.8 GPa for $\langle 111 \rangle \{110\}$. The energy curves for the two systems also have the same maximum. These results, which are common in bcc metals, have their origin in the symmetry of the "saddle point" structures that govern the shear strength [7,10]. The saddle point structures for the two slip systems are identical. Moreover, the saddle point structure in shear is precisely the bct saddle point structure that governs the

orthorhombic instability in tension. The convergence of the three strain paths to the same saddle point simply shows that the nearby saddle points on the energy hypersurface act as "attractors" to which the various deformations are drawn.

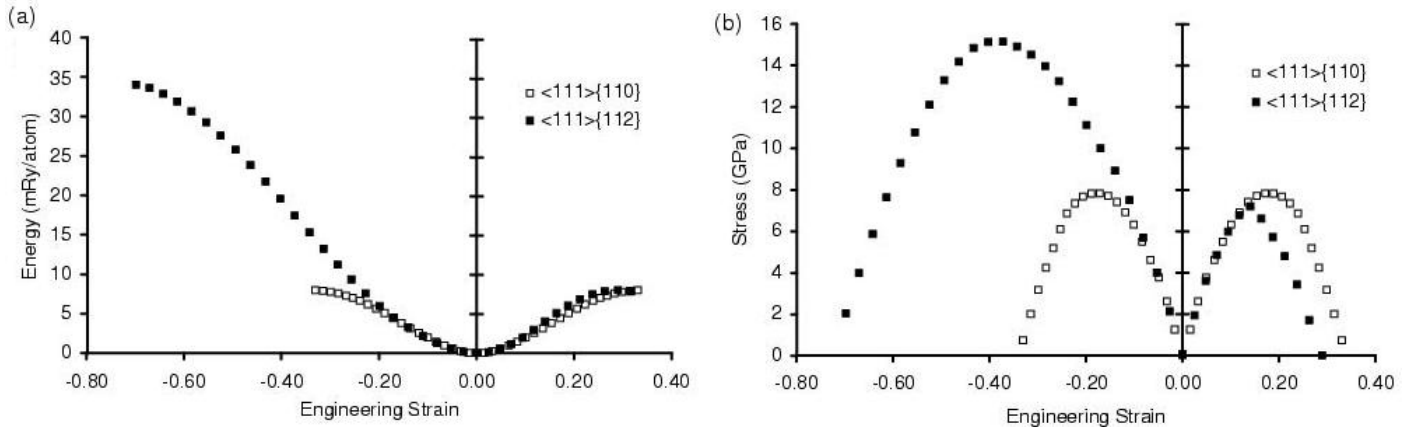


Figure 8: (a) Energy versus shear strain and (b) absolute value of the stress versus strain for (filled square) $\langle 111 \rangle \{112\}$ shear and (open square) $\langle 111 \rangle \{110\}$ shear.

Table 2

Summary of stresses and strains associated with instabilities and saddle points. The tensile strains are referred to a bct cell with the [001] axis along the z-axis. For $\langle 111 \rangle \{112\}$ shear, the reference structure is a base centered monoclinic cell with its 2-fold axis parallel to the x-axis, one orthogonal lattice vector parallel to the shear direction which coincides with the y-axis, and the other orthogonal lattice vector in the y-z plane. For $\langle 111 \rangle \{110\}$ shear, the reference structure is a triclinic cell with one lattice vector in the shear direction which coincides with the y-axis, the second lattice vector in the shear plane which coincides with the x-y plane, and third vector with some component in the z-direction.)

	Tension		Shear		
	$\langle 001 \rangle$ tetragonal	$\langle 001 \rangle$ orthorhombic	$\langle 111 \rangle \{112\}$ (hard)	$\langle 112 \rangle \{112\}$ (easy)	$\langle 111 \rangle \{110\}$
σ_m, τ_m (GPa)	12.6	12.6	15.0	7.2	7.8
Instability	bct	bct	monoclinic	monoclinic	triclinic
e_{xx}	-.042	-.049	.037	-.008	-.002
e_{yy}	-.042	-.049	-0.26	-.006	-.001
e_{zz}	.150	.176	.042	.028	.029
γ_{yz}			-.374	.140	.059
γ_{xz}					.020
γ_{xy}					.035
Saddle Point	fcc	bct	orthorhombic	bct	bct
e_{xx}	-.091	-.070	.046	.004	-.014
e_{yy}	-.091	-.070	-.031	-.016	-.015
e_{zz}	.286	.209	.088	.044	.033
γ_{yz}			-.726	.288	.339
γ_{xz}					.022
γ_{xy}					.154

While the saddle point structure for the two slip systems is the same, the strain paths on the energy hypersurface are slightly different. This difference is responsible for the fact that the strain at which the bct structure occurs is slightly larger for the $\langle 111 \rangle \{110\}$ system, and the ideal strengths for the two systems

differ by $\sim 8\%$. The relaxation of the crystal lattice during strain is also distinctly different. A constant volume shear on the $\langle 111 \rangle \{112\}$ system (with no relaxation in the slip plane) produces a body centered orthorhombic structure at a engineering shear strain of 33%. Allowing relaxation, the special bct structure is reached after a strain of 29% with a 4% expansion perpendicular to the slip plane, and relaxation strains in the slip plane of $< 2\%$ (see Fig. 8 and Table 2). On the other hand, a $\langle 111 \rangle \{110\}$ shear reaches the bct structure at 34% strain, but requires a significant relaxation in the slip plane, the largest component being a 15% shear. The reason for the differences between $\{112\}$ and $\{110\}$ shear lies in the fact that while both paths begin at bcc and end at the bct saddle-point structure, the very different applied stresses cause them to diverge from one another at intermediate strains and produce significantly different atomic configurations near the point of instability.

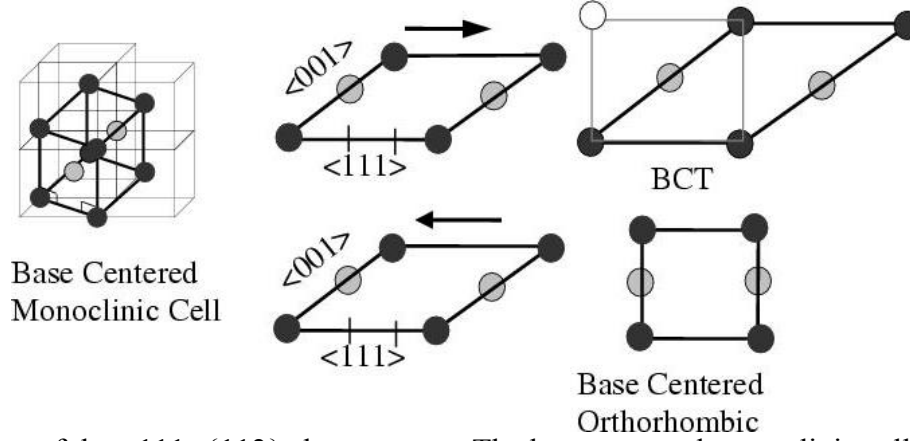


Figure 8: Geometry of the $\langle 111 \rangle \{112\}$ shear system. The base centered monoclinic cell is shown inside the initial bcc structure (left). A $\{110\}$ projection of the structure shows the how the monoclinic cell becomes a bct cell upon applying a $\sim 33\%$ shear in the easy direction (top). A shear in the opposite (hard) direction generates a base centered orthorhombic structure after a shear strain of $\sim 66\%$ (bottom). The monoclinic structure's two fold axis is pointed out of the page. Black atoms are those in the closest plane and the gray atoms are in the following plane of atoms.

As suggested by Frenkel [25], we model the ideal strength by assuming the that the stress-strain relation is sinusoidal with an amplitude τ_m and period $2 \gamma_B$:

$$\tau = \tau_m \sin(\gamma \pi / \gamma_B). \quad (3)$$

If we require that Hooke's law be satisfied for small strains, this implies that

$$\tau_m = \gamma_B G_{\langle 111 \rangle} / \pi, \quad (4)$$

where $G_{\langle 111 \rangle}$ is the shear modulus in the $\langle 111 \rangle$ direction. (Note that the shear moduli are the same for both shear systems.) If we take γ_B to be 0.34, then Eq. 4 predicts $\tau_m = 0.11 G_{\langle 111 \rangle}$. Our results give dimensionless strengths which are very close to this, for $\{112\}$ $\tau_m/G=0.11$ and for $\{110\}$ $\tau_m/G=0.12$, where we have used the experimental value of $G_{\langle 111 \rangle}$ from Table 1. Using the calculated value of $G_{\langle 111 \rangle}$ the reduced strengths are 0.10 and 0.094 for shear on the $\{112\}$ and $\{110\}$ planes respectively.

The shear strength in the hard direction for the $\langle 111 \rangle \{112\}$ system is 15.0 GPa. It follows a path toward a different saddle point that is much higher in energy (see Figs. 7 and 8). The saddle point structure is base centered orthorhombic with an $a:b:c$ ratio of 1:1.06:1.77. This structure can also be pictured as a simple tetragonal structure with a c/a ratio of 2.42 that has undergone an (engineering) shear strain of 6% in the plane perpendicular to the unique axis. Figure 9 demonstrates the geometry and the fact that the strain needed to reach this saddle point is approximately twice that for shear in the easy direction.

To test the numerical accuracy of the PAW method, the energies of several structures along the $\langle 111 \rangle \{112\}$ "easy" shear path were also computed with the FLAPW technique. The energy differences were less than 0.2

mRy. While we have not confirmed that the stress states of these structures are uniaxial when computed with the FLAPW method, the close agreement in the energies along the deformation path suggests that the PAW method is quite accurate in this regime.

Magnetic instabilities

We also investigated the possibility that finite shear strain would induce magnetic instabilities that would limit the shear strength. This was done by testing several different magnetic structures and relaxing the stresses, as in the ferromagnetic case. The energy was only computed at a few interesting points along the $\langle 111 \rangle \{112\}$ loading path. The magnetic structures were chosen to mimic the DAFM structure used for the tensile strength calculations, but because the crystal is monoclinic along the loading path, there are several inequivalent ways of arranging the up and down spins in such a fashion. The 5 structures we studied are shown in Fig. 9. They include superlattices made up of one or two base centered monoclinic cells, with different arrangements of the up and down spins occupying the sites.

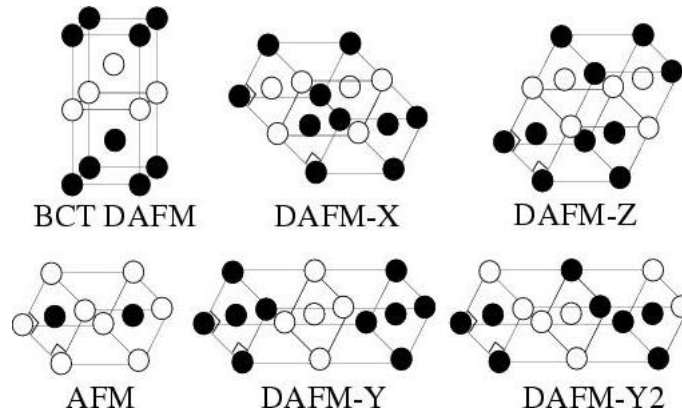


Figure 9: The magnetic structures used to describe complex magnetic ordering in $\langle 111 \rangle \{112\}$ shear. The structures are supercells made up of 1 or 2 body centered monoclinic cells whose 2-fold axes are oriented out of the page. The bct-DAFM structure is shown for reference.

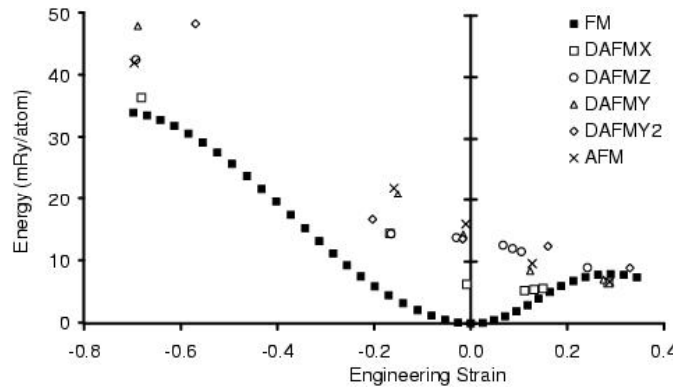


Figure 10: Energy as a function of shear strain for several magnetic structures. (solid square) FM, (open square) DAFMX, (open circle) DAFMZ, (open triangle) DAFMY, (open diamond) DAFMY2, (X) AFM.

Fig. 10 shows the energy as a function of strain for the relaxed structures. There is a magnetic transformation at $\sim 20\%$ strain to the magnetic structure denoted DAFMX. However, this strain is beyond the point of elastic instability, so this transformation does not affect the ideal shear strength. The energy as a function of strain for the DAFMX structure was confirmed by FLAPW calculations using a method similar to that described above. We again note that we have only considered here a set of collinear structures which we hope approximate the ground state magnetic structure; however, the introduction of non-collinear magnetic ordering may further reduce the energy of some of these structures.

IDEAL STRENGTH IN MULTIAXIAL LOADING

The previous two sections have described the ideal strength of iron under simple loading configurations: uniaxial tension and pure shear. However, in many engineering applications the stress state experienced by a material is more complex. In this section we study the strength of iron for uniaxial tension in the [001] direction in combination with biaxial tension or compression in the (001) plane. The case of unbalanced triaxial tension is commonly encountered in front of a crack tip and is thus of practical importance.

The ideal strength calculations were carried out in a manner similar to that used for uniaxial tension; however, in this case the structure is relaxed to achieve the multiaxial stress state desired. For triaxial tension the stress state was taken to be $\sigma_{11}=2\sigma_{22}=2\sigma_{33}$ while for uniaxial tension plus biaxial compression the stress state was taken to be $\sigma_{11}=-\sigma_{22}=-\sigma_{33}$. In practical terms, the desired stress state was said to be achieved when the Hellman-Feynman stresses obeyed the above equalities to within 0.1 GPa.

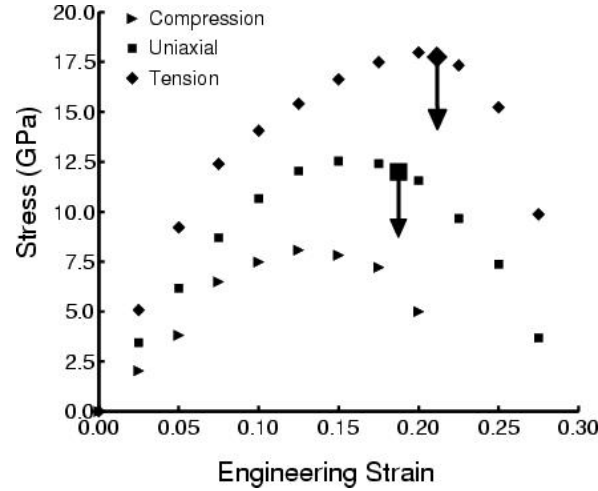


Figure 11: Stress as a function of strain for FM Fe under three different multiaxial loads: uniaxial tension plus biaxial compression (triangle), uniaxial tension (square), triaxial tension (diamond). In all cases the largest tensile stress is in the [001] direction. The large symbols with arrows indicate the location of tetragonal to orthorhombic instabilities. (The load configuration that includes biaxial compression was not tested for this type of instability.)

The weak direction in tension for bcc metals is known to be the $\langle 001 \rangle$ direction, so we focus our attention on this orientation. Fig. 11 shows the stress as a function of engineering strain in the $\langle 001 \rangle$ direction for the three different stress states considered. We see that the application of a tensile stresses perpendicular to the primary tensile direction raises the ideal tensile strength while compressive stresses decrease the ideal strength. In conjunction with this we note that the strain corresponding to the ideal strength is increased in the tensile case and decreased in the compressive case.

These results are in contrast to the often held assumption that the tensile strength of a material should decrease in a triaxial stress state. However, the reason for this result becomes clear if one examines the effect of these stresses from the perspective of their associated strains. The application of a [001] tensile strain to a bcc metal causes the symmetry to be broken and the crystal structure becomes body centered tetragonal (bct). When the c/a ratio of the bct crystal is increased to $\sqrt{2}$ it becomes the fcc structure. Cubic symmetry requires that the [001] tensile stress vanish for both the bcc and fcc structures (at least, if we ignore the magnetic effect, which is small). As such, these structures are symmetry-induced extrema (or saddle points) on the multidimensional energy-strain surface.

We can model the stress-strain curve between the two energy extrema by a sinusoid as suggested by Orowon [9]:

$$\sigma = \sigma_m \sin(e \pi / e_{\max}), \quad (5)$$

where σ_m is the ideal strength, e is the engineering strain, and e_{\max} is the engineering strain of the second stress-free structure. Requiring that the Hooke's law be obeyed at small strain, one finds that

$$\sigma_m = e_{\max} E_{\langle 001 \rangle} / \pi, \quad (6)$$

where $E_{\langle 001 \rangle} = 1/s_{11}$ is the Young's modulus in the $\langle 001 \rangle$ direction.

Now consider the effect of the triaxial stress state on the bct structure. The addition of the orthogonal tensile stresses increases the length of the crystal in the $[100]$ and $[010]$ directions. Because of this, a larger strain is needed in the $[001]$ direction to reach the fcc structure, increasing e_{\max} . Given this, Eq. 6 implies that the ideal strength should be increased in tension. In a similar way, the addition of compressive stresses orthogonal to the tensile direction will have the opposite effect and decrease the strain needed to reach the fcc saddle point structure. In this analysis we have assumed that the stress-strain curve remains sinusoidal under multiaxial loads.

An additional effect not explicitly included in Equation 6 is caused by the pressure dependence of the Young's modulus. It would be possible for triaxial tensile stresses to lower the ideal tensile strength of a bcc metal if the additional stresses decreased the Young's modulus more than they increased the strain needed to reach the fcc structure. From the initial slopes in Fig. 11, we see that triaxial tensile stresses increases the Young's modulus in iron, which increases the ideal strength even more than if the Young's modulus were independent of pressure. This increase in the Young's modulus with pressure is consistent with the experimentally determined pressure dependence of the elastic constants [26].

As discussed in above, the body centered tetragonal structure can become elastically unstable with respect to transformation to a face centered orthorhombic structure. For uniaxial tension in iron, this shear failure occurs at strains larger than the elastic instability associated with the tetragonal Bain path. We find that the triaxial stress state studied here increases the strain at which the tetragonal to orthorhombic transition occurs; however, the increase is less than the increase in the strain associated with the peak in the stress-strain curve (see Fig. 11). The effect is to cause the orthorhombic instability to occur closer to the maximum in the stress-strain curve of the tetragonal structure for triaxial tension.

We have not studied the effect of pressure on the magnetic transformations that can occur along the Bain path. In the uniaxial case, the elastic instability occurs at smaller strains than these magnetic transitions and thus it dictates the ideal strength. To a first order we expect that the addition of orthogonal tensile stresses would enhance the stability of the ferromagnetic phase due to a narrowing of the bandwidth, while the addition of compressive stresses would tend to favor antiferromagnetic or non-spin polarized (paramagnetic) phases. This suggests that even under multiaxial loading the ideal strength is governed by the elastic instability rather than the magnetic instability; however, a more detailed study would be needed to verify this claim as it is not known whether the change in the strain associated with the magnetic phase transitions would be larger or smaller than the change in the strain associated with the elastic instability.

CONCLUSIONS

Ab initio total energy calculations using the PAW method were used to calculate the ideal strength of iron in tension and shear. The ideal tensile strength in the $\langle 001 \rangle$ direction is 12.6 GPa and is associated with an elastic instability at 15% strain along the Bain path from bcc to fcc. At this strain the structure is stable with respect to both orthogonal elastic instabilities and magnetic instabilities. However, if it were possible to reach larger strains, both an elastic instability toward a face centered orthorhombic structure occurs and a magnetic instability from the bct FM to a DAFM magnetic structure would be encountered.

The ideal shear strengths of the two shear systems, $\langle 111 \rangle \{112\}$ and $\langle 111 \rangle \{110\}$, are 7.2 GPa and 7.8 GPa respectively. The ideal shear strengths are very similar because they are determined by the same body-centered tetragonal "saddle point structure". (This bct "saddle-point structure" is also responsible for the orthorhombic instability in tension). Along the $\langle 111 \rangle \{112\}$ shear path, a magnetic instability toward a complex magnetic structure is found at ~20% strain. Like the magnetic instabilities in tension, it does not

compromise the ideal strength because it occurs at larger strains than the elastic instability in the ferromagnetic phase.

The ideal tensile strength in the $\langle 001 \rangle$ direction is increased when one applies a biaxial tensile stress in the (001) plane while the strength is decreased when the additional stress is biaxial compression. This effect can be understood based on a simple crystallographic model. The triaxial stress state increases the strain needed to reach the fcc saddle point structure, which results in a higher strength. The tetragonal to orthorhombic instability is found to move closer to the peak in the stress strain curve, a result similar to what is found in Nb despite the fact that they undergo different failure modes under uniaxial tension.

Despite its complex magnetic behavior and its metastable fcc phase, the ideal strength of Fe is governed by the same elastic instabilities that are found in typical bcc transition metals like W and Mo.

ACKNOWLEDGEMENTS

This work was supported by the Director, Office of Science, Office of Basic Energy Sciences, Division of Materials Sciences and Engineering, of the U.S. Department of Energy under Contract No. DE-AC03-76SF00098.

REFERENCES

1. A. Kelly and N. H. MacMillan (1986). *Strong Solids*. Clarendon Press, Oxford, 3rd ed. pp. 1-56.
2. J. W. Morris Jr., C. R. Krenn, D. Roundy, and Marvin L. Cohen (2000). In: *Phase Transformations and Evolution in Materials*. P. E. Turchi and A. Gonis (eds.). TMS, Warrendale, PA., pp.187-207.
3. D. M. Clatterbuck, D. C. Chrzan, and J. W. Morris Jr. (2002). *Phil. Mag. Lett.* **82**, 141.
4. D. M. Clatterbuck, D. C. Chrzan, and J.W. Morris Jr. (2003). *Acta Materialia*, **51**,2271.
5. M. Sob, L. G. Wang, and V. Vitek (1998). *V. Kovove Materialy* **36**, 145.
6. M. Sob, L. G. Wang, and V. Vitek (1997). *Mat. Sci. Eng. A* **234-236**, 1075.
7. W. Luo, D. Roundy, M. L. Cohen, and J. W. Morris Jr. (2002). *Phys. Rev. B* **66**, 094110.
8. F. Milstein and J. Marschall (1988). *Phil. Mag. A* **58**, 365.
9. E. Orowan (1949). *Rept. Prog. Phys.* **12**, 185.
10. D. Roundy, C. R. Krenn, Marvin L. Cohen, and J. W. Morris Jr. (2001). *Phil. Mag. A* **81**, 1725.
11. H. C. Herper, E. Hoffman, and P. Entel (1999). *Phys. Rev. B* **60**, 3839.
12. D. J. Singh, W. E. Pickett, and H. Krakauer (1991). *Phys. Rev. B* **43**, 11628.
13. D. J. Singh (1994). *Planewaves, Pseudopotentials and the LAPW Method*. Kluwer Academic, Boston
14. P. E. Blochl (1994). *Phys. Rev. B* **50**, 17853.
15. D. Roundy, C. R. Krenn, Marvin L. Cohen, and J. W. Morris Jr. (1999). *Phys. Rev. Lett.* **82**, 2713.
16. B. D. Cullity (1972). *Introduction to Magnetic Materials*. Addison-Wesley, Reading Mass., p 617
17. Y. Tsunoda (1989). *J. Phys. Condens. Matter* **1**, 10427.
18. Y. Tsunoda, Y. Nishioka, R. M. Nicklow (1996). *J. Magn. Mag. Mat.* **128**, 133.
19. K. Knopfle, L. M. Sandratskii, and J. Kubler (2000). *Phys. Rev. B* **62**, 5564.
20. M. Acet, H. Zahres, E. F. Wassermann, and W. Pepperhoff (1994). *Phys. Rev. B* **49**, 6012.
21. J. A. Rayne and B. S. Chandrasekhar (1961). *Phys. Rev.* **122**, 1714.
22. L. Stixrude, R. E. Cohen, and D. J. Singh (1994). *Phys. Rev. B* **50**, 6442.
23. M. Friak, M. Sob, V. Vitek (2001). In: *Proc. Int. Conf. Juniormat 2001*, Institute of Materials Engineering, Brno University of Technology, Brno, p. 117
24. S. S. Brenner (1956). *J. Appl. Phys.* **27**, 1484.
25. J. Frenkel (1926). *Z. Physik* **7**, 323.
26. F. Nelson (ed.) (1992). *Landolt-Bornstein LBIII/29a -- Low Frequency Properties of Dielectric Crystals: Second and Higher Order Elastic Constants*, Springer-Verlag, Berlin